Diffraction imaging in fractured carbonates and unconventional shales

Ioan Sturzu[1], Alexander Mihai Popovici[1], Tijmen Jan Moser[2], and Sudha Sudhakar[3]

Abstract

Diffraction imaging is recognized as a new approach to image small-scale fractures in shale and carbonate reservoirs. By identifying the areas with increased natural fracture density, reservoir engineers can design an optimal well placement program that targets the sweet spots (areas with increased production), and minimizes the total number of wells used for a prospective area. High-resolution imaging of the small-scale fractures in shale reservoirs such as Eagle Ford, Bakken, Utica, and Woodbine in the US, and Horn River, Montney, and Utica in Canada improves the prospect characterization and predrill assessment of the geologic conditions, improves the production and recovery efficiency, reduces field development cost, and decreases the environmental impact of developing the field by using fewer wells to optimally produce the reservoir. We evaluated several field data examples using a method of obtaining images of diffractors using specularity filtering that could be performed in depth and time migration. Provided that a good migration velocity was available, we used the deviation of ray scattering from Snell's law to attenuate reflection energy in the migrated image. The resulting diffraction images reveal much of the structural detail that was previously obscured by reflection energy.

Introduction

In regular migration, the information coming from small scattering objects is hidden by the energy of major specular reflectors. By careful preprocessing, the inherent redundancy of prestack seismic data can be used to separate the contribution of high-energy specular events from those of low-amplitude events scattered by local unconformities and heterogeneities. Because diffractors are, by definition, smaller than the seismic wavelength, diffraction imaging provides a key to superresolution information, which consists of image details that are beyond the classical Rayleigh limit of half a seismic wavelength. The importance of diffractions in high-resolution structural imaging has been emphasized in many recent publications (Khaidukov et al., 2004; Kozlov et al., 2004; Fomel et al., 2006; Landa et al., 2008; Moser and Howard, 2008; Moser, 2009; Klokov et al., 2010; Dell and Gajewski, 2011; Koren and Ravve, 2011; Klokov and Fomel, 2012; Decker et al., 2013; Popovici et al., 2014; Sturzu et al., 2014), and diffraction imaging is emerging as a new tool in seismic interpretation. In fact, most standard seismic processing steps enhance specularity and suppress diffracted energy (interpolation, FXY deconvolution, and *f-k* filtering, binning). The objective of diffraction imaging is not to replace traditional processing, but rather to provide interpreters with complementary additional 3D or 4D volumes to fill in the small, but potentially crucial, structural details. Images with increased resolution allow seismic data to be used more effectively in characterization and delineation of oil and gas reservoirs and monitoring of enhanced oil recovery processes, thereby reducing the risk of drilling mistakes.

Techniques for diffraction imaging fall into two categories. In the first category are methods that separate the seismic data into two parts, one that contains the wave energy from reflections (specular energy) and the other that contains the wave energy from diffractions. Each component is used to provide an image through traditional seismic imaging methods. In the second category are methods that do not separate the seismic data before, but during the migration. Moser and Howard (2008) and Moser (2009) extract the local direction of specularity from a previously obtained migration stack, and they use this information during a subsequent migration step to filter out events that satisfy Snell's law. Specularity gathers (Sturzu et al., 2013, 2014) are very effective in selecting filter parameters after migration.

In this paper, we briefly outline the technique behind diffraction imaging and present several case studies, with particular attention to application on optimized well planning.

[1]Z-Terra Inc., Houston, Texas, USA. E-mail: isturzu@z-terra.com; mihai@Z-Terra.com.
[2]Moser Geophysical Services, The Hague The Netherlands. E-mail: mosertj@gmail.com.
[3]Vector Seismic, Houston, Texas, USA. E-mail: sudha@vector-seismic.com.

Manuscript received by the Editor 15 April 2014; revised manuscript received 26 August 2014; published online 7 January 2015. This paper appears in *Interpretation*, Vol. 3, No. 1 (February 2015); p. SF69–SF79, 12 FIGS.
http://dx.doi.org/10.1190/INT-2014-0080.1.

Diffraction imaging

Standard migration

For a better understanding of diffraction imaging, we briefly summarize the principles of standard Kirchhoff migration; details can be found in Moser and Howard (2008) and Sturzu et al. (2013, 2014). Kirchhoff migration propagates the energy of all seismic data trace to all possible reflection points in a model space describing the elastic properties of the subsurface. After all events on all traces are propagated, an image is generated by stacking all individual contributions. The propagation of these events is performed by organized ray tracing, in the form of traveltime tables. The stack ensures that in-phase energy corresponding to the true reflectors is reinforced, whereas out-of-phase energy is canceled out by destructive interference. This process can be expressed as

$$V(\mathbf{x}) = \int \mathrm{d}t\ \mathrm{d}\mathbf{s}\ \mathrm{d}\mathbf{r}\ U''(t, \mathbf{s}, \mathbf{r})\delta(t - T(\mathbf{s}, \mathbf{x}, \mathbf{r})), \quad (1)$$

where δ is the Dirac delta function; $U''(t, \mathbf{s}, \mathbf{r})$ is the (second time derivative) prestack data, depending on time t and shot/receiver positions $\mathbf{s}/\mathbf{r}$; $T(\mathbf{s}, \mathbf{x}, \mathbf{r})$ is the traveltime computed in the given reference velocity model from $\mathbf{s}$ to $\mathbf{r}$ via the subsurface image point $\mathbf{x}$; and $V(\mathbf{x})$ is the resulting migrated image. The sum (integral) is carried out over the time samples and all source and receiver pairs $(\mathbf{s}, \mathbf{r})$ in the given acquisition.

Specularity

In the subsurface, the discontinuities of the elastic parameters — generally called reflectors — can either be smooth surfaces or locally rough ones. The roughness of a reflecting surface is a result of small discontinuities like structural edges or tips. Smooth reflectors act as a (specular) mirror for seismic energy, which reflects on them following Snell's law: The angles of incidence and reflection are equal. On the other hand, diffractions on small discontinuities do not follow Snell's law. Therefore, the agreement with Snell's law, or specularity, can be used as a discriminator between reflections and diffractions.

Geometrically, we define specularity S as the (cosine of the) angle between the local reflector (unit) normal $\mathbf{n}$ and the bisector of incoming and reflected rays. Because this bisector is parallel to the gradient of the total traveltime with respect to the image point $\mathbf{x}$, $T_{\mathbf{x}}$, we have

$$S(\mathbf{s}, \mathbf{x}, \mathbf{r}) = |\mathbf{n} \cdot T_{\mathbf{x}}| / \|T_{\mathbf{x}}\|, \quad (2)$$

where the dot denotes the scalar product. By this definition, the specularity depends on the location of the image point $\mathbf{x}$, but also on the source $\mathbf{s}$ and receiver $\mathbf{r}$ contributing to the image there. For specular reflections on a strong reflector $S = 1$ ($\mathbf{n}$ and $T_{\mathbf{x}}$ are collinear), for nonspecular diffractions $S < 1$ ($\mathbf{n}$ and $T_{\mathbf{x}}$ make a nonzero angle).

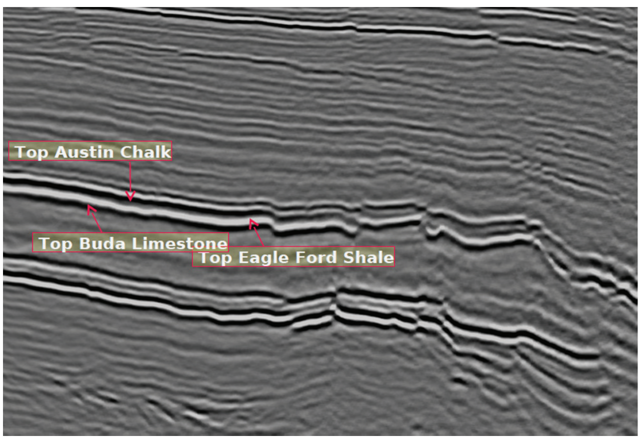

Figure 1. Eagle Ford Horizons on standard prestack depth migration image (data are courtesy of Seitel).

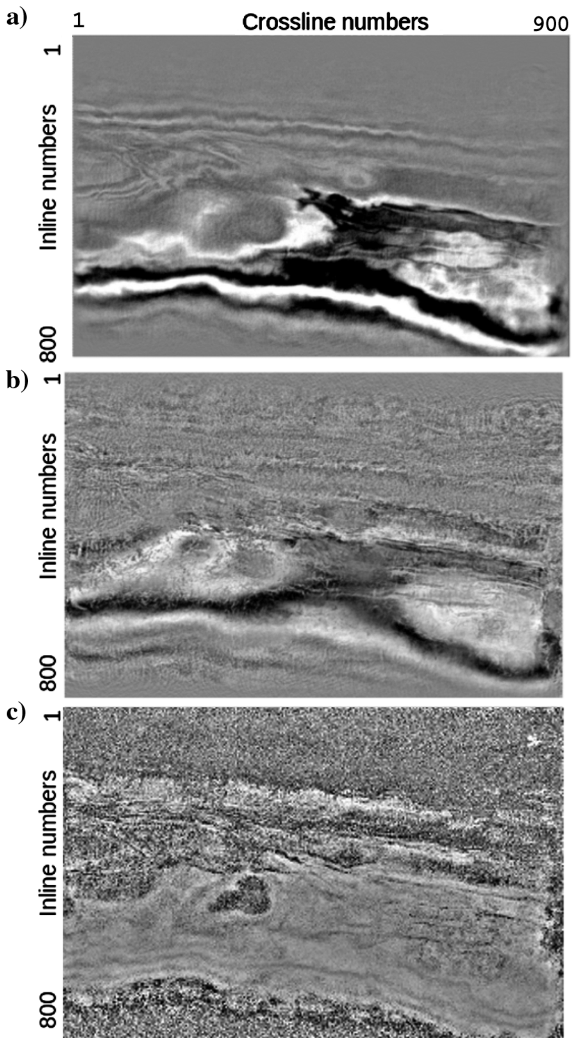

Figure 2. Depth slices over Eagle Ford at 4023 m (13,200 ft): (a) standard depth migration, (b) diffraction image, and (c) coherence (data are courtesy of Seitel).

A straightforward procedure for obtaining a diffraction image is outlined in Moser and Howard (2008) and Moser (2009). First, using standard Kirchhoff migration, we obtain the seismic image; this image will include reflections and diffractions, with the reflections dominating the image. The second step is to analyze the structural reflectors in the Kirchhoff image and determine the normal vector **n** to them at each image point (reflector dip extraction). This step assumes an optimally focused image obtained with the best velocity model, so the information extracted is accurately related to the geologic geometry of the subsurface. In a second migration run, the migrated seismic events are stacked using a weighting factor designed to attenuate the contribution of the specular events and preserving diffractors.

A special ingredient in the second migration step, called specularity gathers, makes it possible to construct the specularity filter after, rather than before the migration (Sturzu et al., 2013). The idea is to sort the prestack migration output with respect to the specularity S in a way that is similar to an offset or angle common image gather. This can be expressed as

$$V_{sg}(\mathbf{x}, S) = \int \mathrm{d}t\ \mathrm{d}\mathbf{s}\ \mathrm{d}\mathbf{r}\ U''(t, \mathbf{s}, \mathbf{r})\delta(t - T(\mathbf{s}, \mathbf{x}, \mathbf{r})) \times \delta(S - |\mathbf{n} \cdot T_{\mathbf{x}}|/\|T_{\mathbf{x}}\|), \quad (3)$$

with the same notation as in equation 1, except that the migrated image $\mathbf{V}(\mathbf{x})$ in equation 1 now depends on the extra parameter S. In a postprocessing technique similar to the mute and stack of the offset gathers, the diffraction image V_d is obtained by a weighted stack over all the specularity values between zero and one:

$$V_d(\mathbf{x}) = \int_0^1 \mathrm{d}S\ w(\mathbf{x}, S) V_{sg}(\mathbf{x}, S). \quad (4)$$

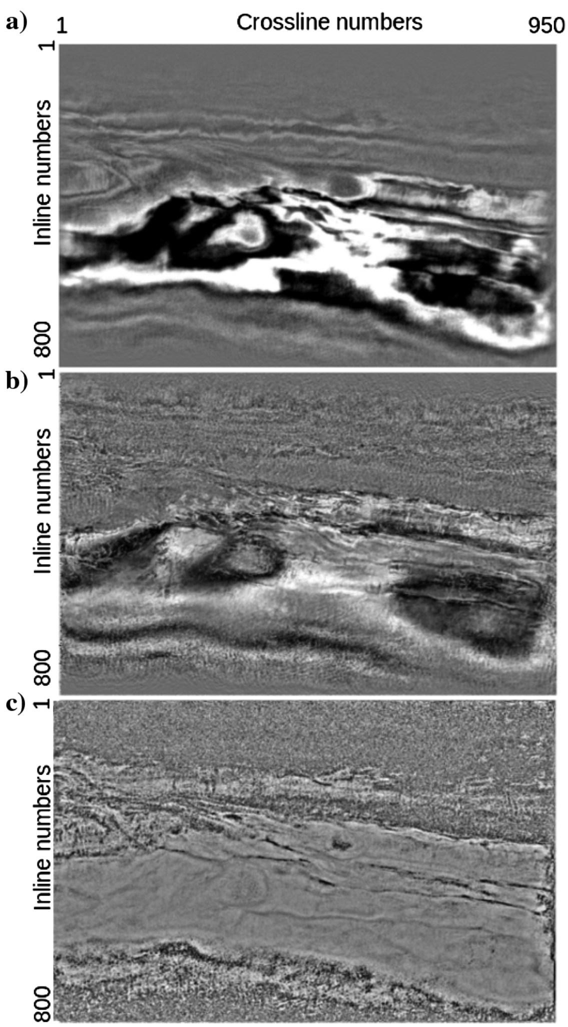

Figure 3. Depth slices over Eagle Ford at 4115 m (13,500 ft): (a) standard depth migration, (b) diffraction image, and (c) coherence (data are courtesy of Seitel).

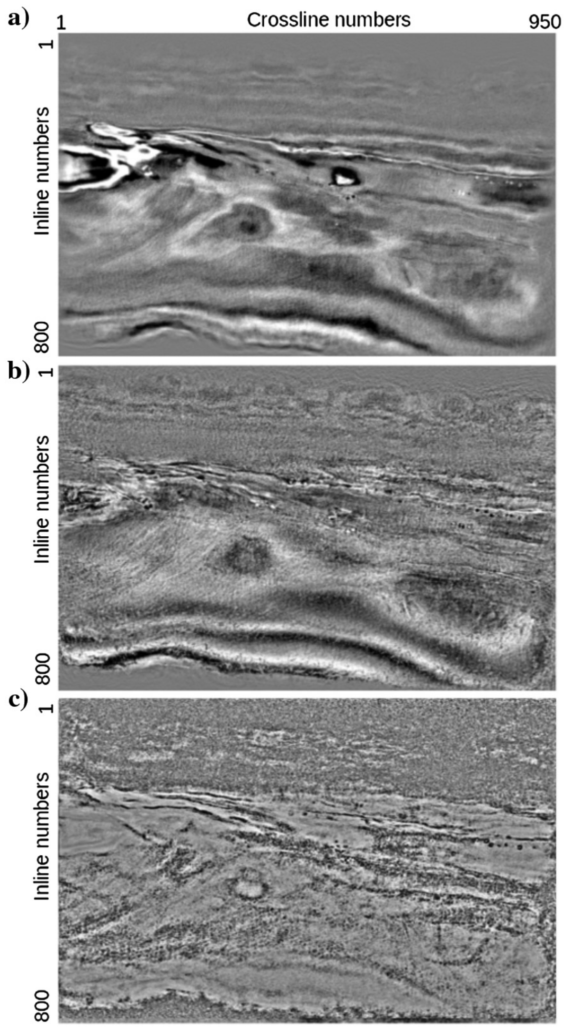

Figure 4. Depth slices over Eagle Ford at 4389 m (14,400 ft): (a) standard depth migration, (b) diffraction image, and (c) coherence (data are courtesy Seitel).

The crux of diffraction imaging is to design the weighting function w so that it is one for $S < 1$ and zero for $S = 1$ with a smooth transition in between (Sturzu et al., 2013). As stated, the use of specularity gathers has the advantage that the weighting function is designed after migration and therefore is constructed, and updated, very efficiently. In particular, the weighting function can be spatially variable ($w = w(\mathbf{x}, S)$) and adapted to the local Fresnel zone width, which is difficult to estimate a priori, but straightforward after migration using specularity gathers. Also, feedback from interpretation can be efficiently included in the weighting function, and hence in the final diffraction image.

Note that the dip extraction assumes that at a given subsurface point (region) there is only a single reference specular direction. However, at many areas of interest, e.g., conflicting dips, pinchouts, unconformities, in the vicinity of near vertical faults or salt flanks, there might be several energetic directions. The diffraction imaging by suppression of strong reflection energy with a single reference specular direction is therefore especially designed to preserve these structural elements.

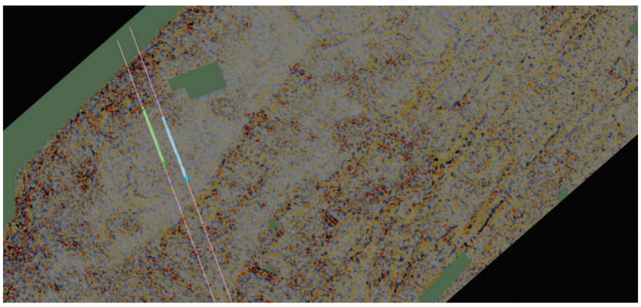

Figure 5. Depth section of Eagle Ford near the top of the chalk level with diffractivity overlain. The well trajectories encounter different patterns of diffractivity amplitude (data are courtesy of Seitel).

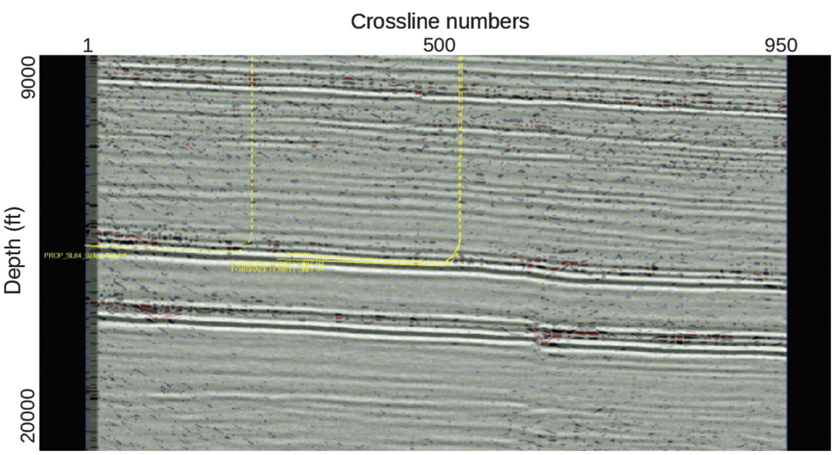

Figure 6. Inline section of Eagle Ford: location of two wells displayed on prestack depth image with diffractivity overlain (data are courtesy of Seitel).

Field data

Eagle Ford shale

As a first field example, we apply the diffraction imaging workflow on the Kenedy 3D survey in the southwestern area of the Eagle Ford play. The diffraction imaging was executed in the framework of prestack depth migration, preceded by preprocessing and prestack time migration (PSTM). Special attention points for a successful diffraction imaging included preprocessing with special care to preserve high-frequency diffraction content and in the depth migration to arrive at an optimal velocity model, allowing optimal focusing of the standard migration image. This process consisted of several tomography iterations. When the velocity model was considered optimal, the resulting standard migration image was used for reflector dip extraction, using a plane wave destructor filter (Fomel, 2002). A typical seismic section is shown in Figure 1. Here, we can observe the high-reflectivity package that includes the Eagle Ford, the overlying Austin Chalk, and the underlying Buda limestone.

The reflector dip field and the traveltime tables of the final velocity iteration were then used for the diffraction imaging. Specularity gather analysis (equation 3) allowed us to efficiently select the best taper parameters to arrive at a high-quality diffraction image. In Figures 2–4, we display a comparison between depth slices obtained using, respectively, (1) the standard depth migration, (2) a diffraction image, and (3) a coherence cube obtained from the migration image using the maximum curvature. Here, we note that the essential difference between the diffraction image and coherence is that the first is obtained prestack and premigration, thus preserving all diffraction information related to small-scale structure. Coherence is produced from the poststack migrated image, where such information is typically lost.

Much work remains to be done to correlate the production to diffractivity. This is especially challenging, given the many factors that affect production. A first step in the process would be to evaluate the correlation between initial production and diffractivity in a qualitative sense. A conceptual example of this is provided in Figures 5 and 6. In Figure 6, we show the paths of two horizontal wells (well A is depicted with green, and well B is shown with blue) and a map view of the diffractivity near the top of the chalk level. The diffractivity is higher at this level than within the Eagle Ford itself, but we might assume that strong diffractivity immediately above the Eagle Ford could indicate fracturing or deformation at the Eagle Ford level itself. We note that well A had a significantly higher initial production rate than well B, which possibly could indicate a correlation to diffractivity. In Figure 5,

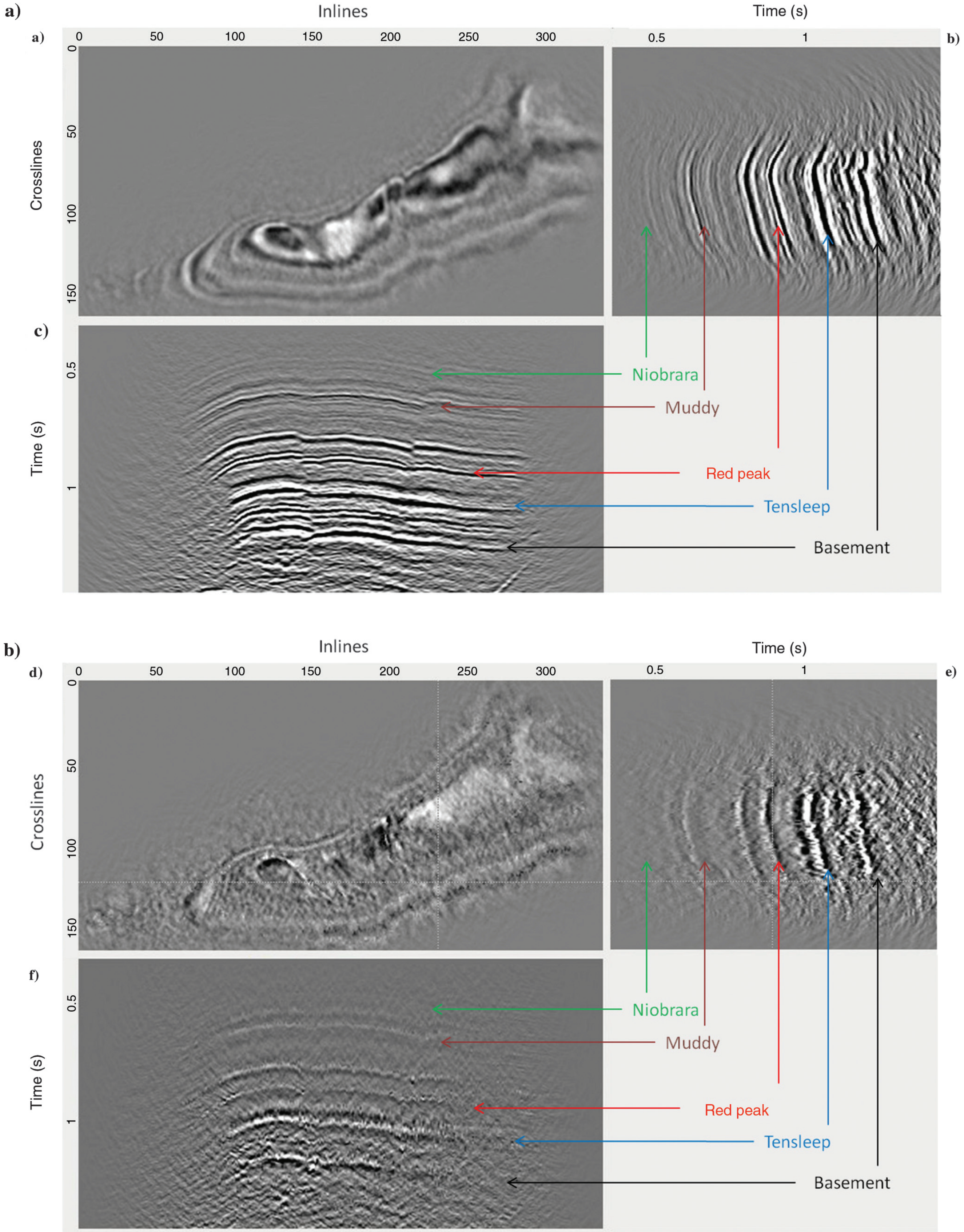

Figure 7. PSTM result for the Teapot Dome data set: (a) time section at 0.888 s, (b) vertical section along line 122, and (c) vertical section along crossline 230. Diffraction image for the Teapot Dome data set: (d) time section at 0.888 s, (e) vertical section along line 122, and (f) vertical section along crossline 230.

we show the trajectories of wells A and B on top of a vertical section.

Teapot dome reservoir

As a second field example, we present the application of the diffraction imaging workflow on the seismic data obtained from the Teapot Dome Reservoir, situated in the southwest part of the Powder River Basin, Wyoming. This site has been extensively studied during the past few decades, and the fact that most of the related data belong to the public domain makes it a useful benchmark in the study of many aspects of petroleum exploration (Cooper et al., 2001; Finn and Johnson, 2005; Friedmann and Stamp, 2005; Milliken and Black, 2006; Raeuchle et al., 2006). The main geologic units clearly visible in the seismic images are the (Upper Cretaceous) Niobrara Shale, the (Lower Cretaceous) Muddy Sandstone, the (Triassic) Red Peak Formation, the (Pennsylvalian) Tensleep Formation, and the (Precambrian) granite basement. The Red Peak Formation is the lower part of the Chugwater Group (Gilbertson, 2002), below the Jelm Formation. According to Gilbertson (2002), Red Peak is Early Triassic in age, deposited in an arid, shallow-marine environment, and is composed primarily of brick-red shales, siltstones, and sandy siltstones. Generally, there is an upward increase in the abundance of coarser grains and an upward increase in the number and thickness of coarser beds (Burk, 1956; Picard, 1993).

The diffraction imaging was run in the framework of PSTM. We used the optimal migration velocity to produce a PSTM stack, which was subsequently used to extract the reflector dips. Using this information, we further remigrated the data and sorted the output in specularity gathers. After applying an appropriate taper to eliminate the specular energy, the gather was stacked into the diffraction image. Diffraction imaging in the time domain requires special considerations to deal with the different physical meaning of the vertical (time) and horizontal dimensions (distance); details are given in Appendix A.

In Figure 7a–7c, we display horizontal and vertical sections through the regular PSTM stack. The horizontal slice is taken at 0.888 s and mainly displays the image of the Red Peak Formation, while the two vertical sections are taken, respectively at representative inlines and crosslines. The main geologic formations are indicated in the image. In Figure 7d–7e. we display the corresponding sections through the diffraction image. For comparison, Figure 8 shows the same time section taken at 0.888 s through a coherency cube calculated using the event similarity prediction algorithm. The main diffractive events in the diffraction image 7d–7e are observable in the coherency cube as well, but with much less detail. In Figure 9, we compare the same results from Figure 7 on a smaller detailed region. Here, one notices a clear pinchout that is revealed only in the diffraction image.

Calibration using well data

We show examples of use of diffraction imaging technology in the Bakken Shale play, in North Dakota and in the Bone Spring play in the Midland basin. Modern wide-azimuth 3D surveys that are typically acquired have good distribution of multiple azimuth directions between the source and receiver positions. Multiazimuth seismic data not only enable superior imaging, but if the azimuthal information is carried correctly through all imaging steps, multiazimuth diffraction imaging techniques using residual traveltimes and amplitudes can be effectively used for reservoir property description. However, the quality of the data conditioning including solving near-surface static model and calibration to wells will result in better diffraction migration images and identification of fracture patterns.

Using dip meter logs, we can confirm the presence of fractures and judge the orientation of fractures. We then calibrate this information against the diffraction-image-generated fracture orientation and fracture density count.

We can then see how these logs relate to diffraction-image-generated fracture patterns. Whole core information can also be used to understand the fracture density and orientations and can be used to calibrate the diffraction imaging output in the same way.

Once calibrated with a few wells the diffraction-imaging volume can be used to quickly identify areas of fracture and the direction of these fracture sets so we can orientate the horizontal drill plans to intersect these fractures. Wells that encounter these fracture patterns perform much better in some areas where secondary porosity is established by these open fractures (Figure 10). The edges of the fracture patterns generate

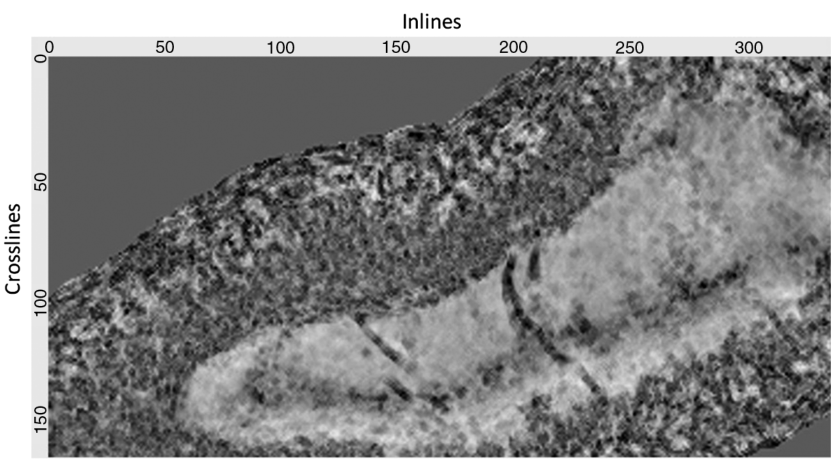

Figure 8. Time slice through the coherency cube for the Teapot Dome data set at 0.888 s. Compare with the diffraction image of Figure 7.

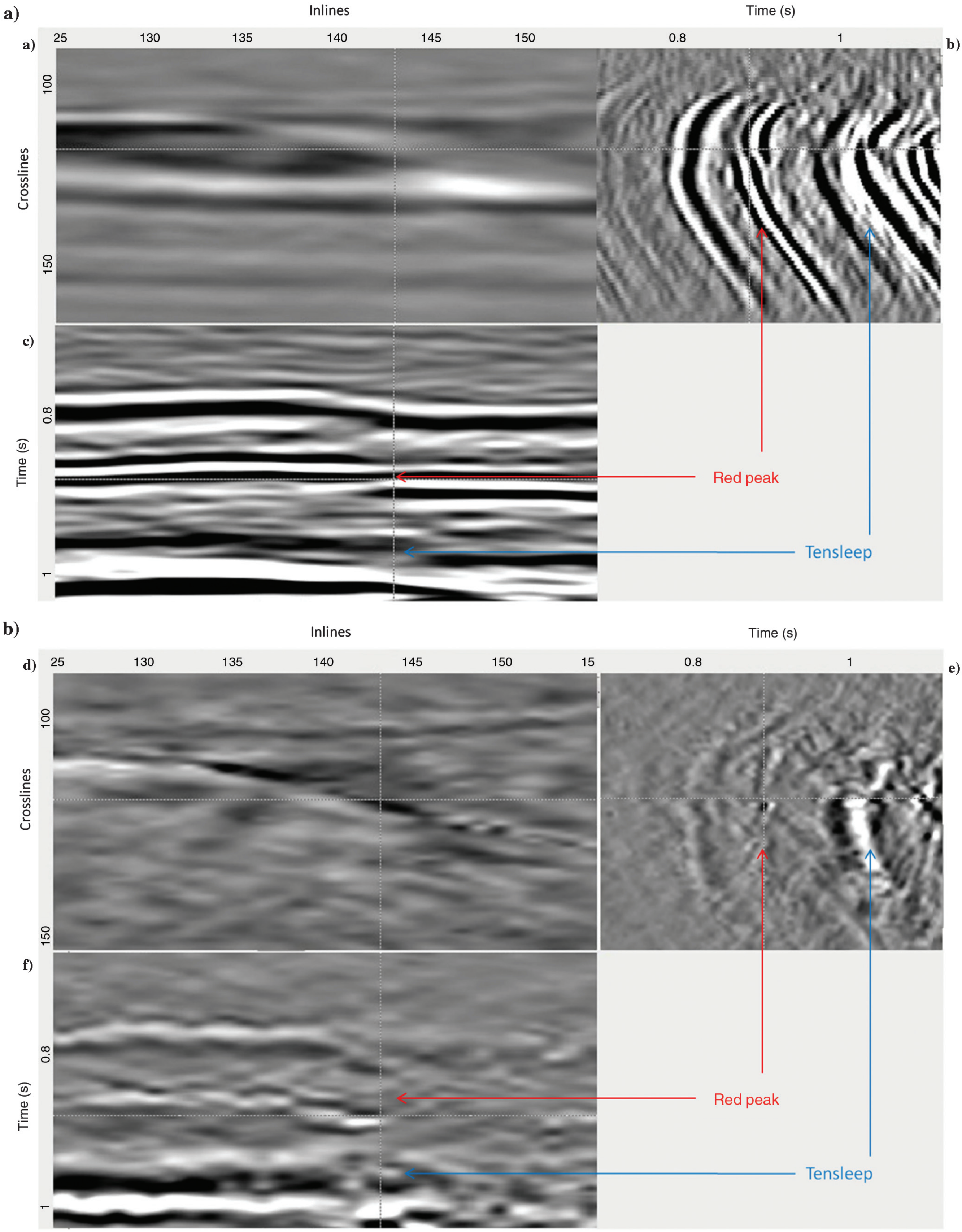

Figure 9. Detail from the PSTM result for the Teapot Dome data set: (a) time section at 0.888 s, (b) vertical section along line 122 (c) vertical section along crossline 230. Detail from the diffraction image for the Teapot Dome data set: (d) time section at 0.888 s, (e) vertical section along line 122, and (f) vertical section along crossline 230.

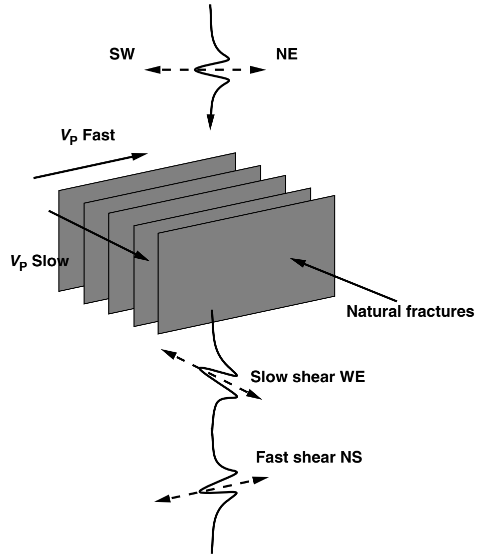

Figure 10. A model of natural fractures. Diffractions can be used to identify areas of fracture and their orientation. NS refers to a generic north–south direction, WE refers to west–east.

one-sided diffraction that remains as residual energy after the diffraction-imaging process.

The coherence and diffraction imaging slice shown in Figure 11 and the magnification in Figure 12 are at the level of the Mississippian Formation at 13,150 ft. This zone is fairly flat and contains reservoir rocks of Mississippian-age primarily weathered carbonate, chert, and sandstone located below a major unconformity. Porosities in the fractured Mississippian average 10% and permeabilities around 55 mD. The 3D seismic data are typically imaged using several passes of prestack depth migration and then calibrated with well logs in the area. The conditioned data are then run through the diffraction imaging process using the updated velocity model. This form of evaluation allows us to pick the best areas for new drilling and also guides us to the orientation of the horizontal wells so as to intersect maximum number of natural fractures.

Figure 11. Comparison of the traditional coherence cube on the top with diffraction imaging patterns generated on the bottom (data are courtesy of Vector Seismic).

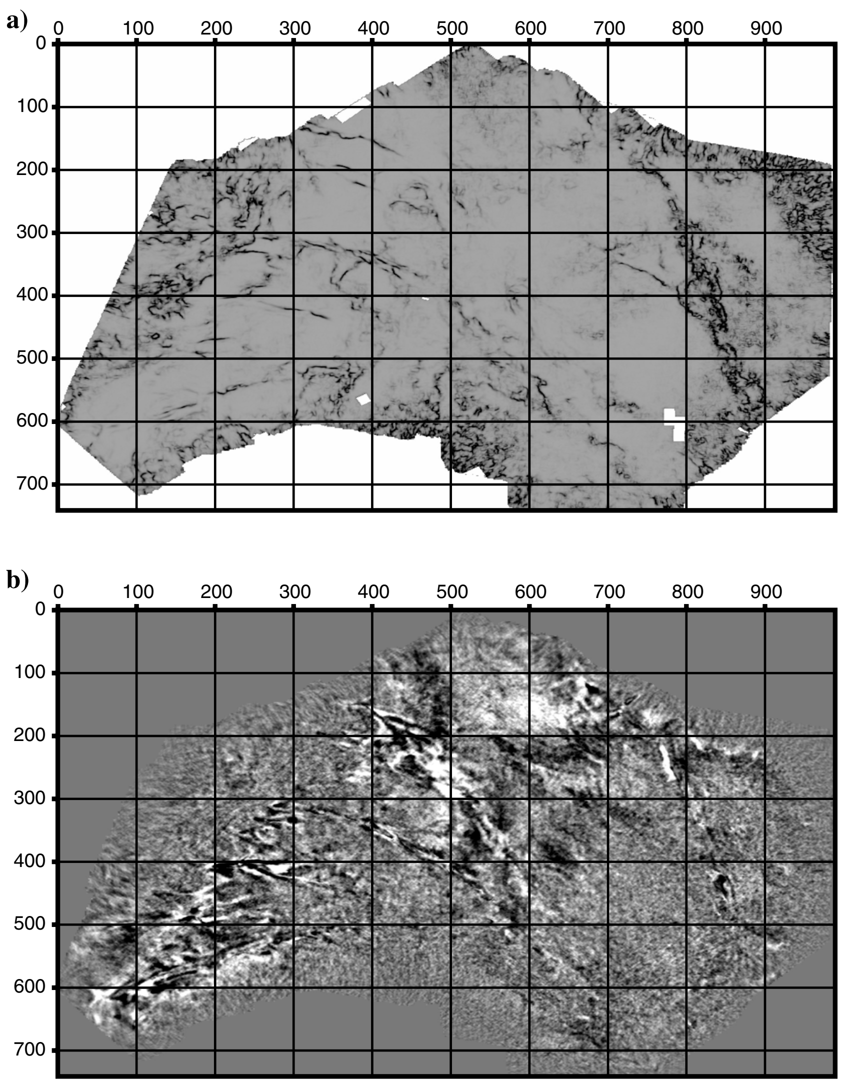

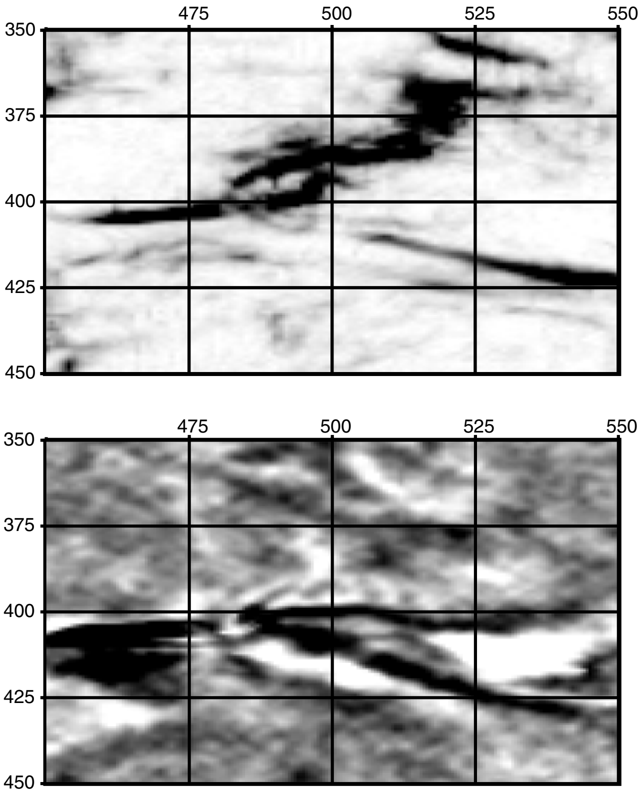

Figure 12. Magnification of Figure 11 (data are courtesy of Vector Seismic).

Conclusions

We present several case studies that reconfirm the potential of diffraction imaging to recover small-scale structural details that are obscured by standard reflection imaging, but that are crucial for the interpretation of shale and carbonate reservoirs. Diffraction imaging has great benefits for the mapping of fractures zones and the determination of their orientation. This has an increasing impact on optimal well planning.

The objective of diffraction imaging is to complement traditional processing and provide interpreters with complementary additional 3D or 4D volumes to fill in the small, but potentially crucial, structural details. Typically, the interpreter will work on the standard reflection image and the diffraction image. The reflection image will provide the main structural skeleton of the subsurface consisting of the strong main reflectors. In addition, the diffraction image enables the interpreter to add high-resolution details, such as fractures.

Acknowledgments

We thank Seitel for permission to show the Eagle Ford data and the Rocky Mountain Oilfield Testing Center and the U.S. Department of Energy for providing the Teapot Dome data set.

Appendix A

Diffraction imaging in the time domain

Kirchhoff time migration is a special and fast migration technique used to obtain a subsurface image. It assumes that the elastic properties do not have severe lateral variations, and it uses vertical propagation traveltime instead of depth as the vertical coordinate in the final image.

The total traveltime T as a function of the image location given by the horizontal spatial coordinates (x, y) and the vertical time coordinate t is expressed as

$$T(x,y,t;x_s,y_s,x_r,y_r) = T_s(x,y,t;x_s,y_s) + T_r(x,y,t;x_r,y_r) = \sqrt{\frac{t^2}{4} + \frac{(x-x_s)^2+(y-y_s)^2}{V_{\mathrm{rms}}^2(t)}} + \sqrt{\frac{t^2}{4} + \frac{(x-x_r)^2+(y-y_r)^2}{V_{\mathrm{rms}}^2(t)}}, \tag{A-1}$$

where (x_s, y_s) and (x_r, y_r) are the horizontal coordinates of the source and receiver and $V_{\mathrm{rms}}(t)$ is the vertical root-mean-square (rms) velocity profile at the midpoint between source and receiver.

The horizontal derivatives of the traveltime are

$$\frac{\partial T}{\partial x} = \frac{x - x_s}{V_{\mathrm{rms}}^2(t)T_s(x,y,t)} + \frac{x - x_r}{V_{\mathrm{rms}}^2(t)T_r(x,y,t)}, \tag{A-2}$$

$$\frac{\partial T}{\partial y} = \frac{y - y_s}{V_{\mathrm{rms}}^2(t)T_s(x,y,t)} + \frac{y - y_r}{V_{\mathrm{rms}}^2(t)T_r(x,y,t)}. \tag{A-3}$$

The vertical derivative of the traveltime is

$$\frac{\partial T}{\partial t} = \frac{t - 4[(x-x_s)^2 + (y-y_s)^2]V_{\mathrm{rms}}{}^{-3}(t)V_{\mathrm{rms}}{}'(t)}{4T_s(x,y,t)} + \frac{t - 4[(x-x_r)^2 + (y-y_r)^2]V_{\mathrm{rms}}{}^{-3}(t)V_{\mathrm{rms}}{}'(t)}{4T_r(x,y,t)}. \tag{A-4}$$

These derivatives are not consistent, in the sense that the horizontal ones have dimensions of time/distance, whereas the vertical ones are dimensionless. As a result, there is a scaling issue when we try to define a reflector normal and specularity following equation 2. To obtain equal dimensions for the traveltime gradient a scaling velocity $V(t)$ is needed:

$$\mathbf{G} = \left(\frac{\partial T}{\partial x}, \frac{\partial T}{\partial y}, \frac{\partial T}{\partial t}\right) \to \mathbf{G}' = \left(\frac{\partial T}{\partial x}, \frac{\partial T}{\partial y}, \frac{1}{V(t)}\frac{\partial T}{\partial t}\right). \tag{A-5}$$

Similarly, for the reflector normal with consistent dimensions a scaling velocity $V(t)$ is needed:

$$\mathbf{N} = (-d_x, -d_y, 1) \to \mathbf{N}' = \left(-d_x, -d_y, \frac{1}{V(t)}\right), \tag{A-6}$$

where d_x and d_y are the components of the reflector dip.

With these notations, the pure specularity condition can be written as ($\times$ denotes the vector cross-product)

$$\mathbf{G} \times \mathbf{N} = \mathbf{0}. \tag{A-7}$$

Expanding this for $\mathbf{G}$, $\mathbf{N}$, and $\mathbf{G}'$, $\mathbf{N}'$ gives

$$\begin{aligned} \mathbf{G} \times \mathbf{N} &= \left(\frac{\partial T}{\partial x}, \frac{\partial T}{\partial y}, \frac{\partial T}{\partial t}\right) \times (-d_x, -d_y, 1) \\ &= \left(\frac{\partial T}{\partial y} + \frac{\partial T}{\partial t} d_y, -\frac{\partial T}{\partial x} - \frac{\partial T}{\partial t} d_x, \frac{\partial T}{\partial y} d_x - \frac{\partial T}{\partial x} d_y\right) \end{aligned} \tag{A-8}$$

and

$$\begin{aligned} \mathbf{G}' \times \mathbf{N}' &= \left(\frac{\partial T}{\partial x}, \frac{\partial T}{\partial y}, \frac{1}{V(t)} \frac{\partial T}{\partial t}\right) \times \left(-d_x, -d_y, \frac{1}{V(t)}\right) \\ &= \left(\left(\frac{\partial T}{\partial y} + \frac{\partial T}{\partial t} d_y\right) \frac{1}{V(t)}, \left(-\frac{\partial T}{\partial x} - \frac{\partial T}{\partial t} d_x\right) \frac{1}{V(t)}, \right. \\ &\quad \left. \frac{\partial T}{\partial y} d_x - \frac{\partial T}{\partial x} d_y\right). \end{aligned} \tag{A-9}$$

From these expressions, it appears that $\mathbf{G} \times \mathbf{N} = \mathbf{0}$ precisely then, when $\mathbf{G}' \times \mathbf{N}' = \mathbf{0}$.

As a result, if the specularity condition (equation A-7) is satisfied (for specular reflection, $S = 1$), then it is satisfied independently from the choice of the reference velocity $V(t)$. When it is not satisfied (for nonspecular diffraction, $0 < S < 1$), there is a velocity-dependent stretch in the S-domain. A proper choice of the weighting factor $w(\mathbf{x}, S)$ then ensures optimal control over the reflection suppression and preservation of diffraction.

REFERENCES

Burk, C. A., ed., 1956, Subsurface stratigraphy of the pre-Niobrara formations in the Wind River Basin, central Wyoming, *in* Wyoming stratigraphy, Part 1: Subsurface stratigraphy of the pre-Niobrara formations of Wyoming: Wyoming Geological Association, 23–33.

Cooper, S. P., J. C. Lorenz, and L. B. Goodwin, 2001, Lithologic and structural controls on natural fracture characteristics Teapot Dome, Wyoming: Technical report DE-A, C04-94AL85000, Sandia National Laboratories.

Decker, L., A. Klokov, and S. Fomel, 2013, Comparison of seismic diffraction imaging techniques: Plane wave destruction versus apex destruction, 83rd Annual International Meeting, SEG, Expanded Abstracts, 4054–4059.

Dell, S., and D. Gajewski, 2011, Common-reflection-surface-based workflow for diffraction imaging: Geophysics, **76**, no. 5, S187–S195, doi: 10.1190/geo2010-0229.1.

Finn, T. M., and R. C. Johnson, 2005, Niobrara total petroleum system in the southwestern Wyoming province, *in* Petroleum Systems and Geologic Assessment of Oil and Gas in the Southwestern Wyoming Province, Wyoming, Colorado and Utah: U.S. Geological Survey, CD-ROM.

Fomel, S., 2002, Applications of plane-wave destruction filters: Geophysics, **67**, 1946–1960, doi: 10.1190/1.1527095.

Fomel, S., E. Landa, and M. Taner, 2006, Poststack velocity analysis by separation and imaging of seismic diffractions, 76th Annual International Meeting, SEG Expanded Abstracts, 2559–2563.

Friedmann, S. J., and V. Stamp, 2005, Teapot Dome: Characterization of a CO_2-enhanced oil recovery site in eastern Wyoming: Environmental Geosciences, **13**, 181–199, doi: 10.1306/eg.01200605017.

Gilbertson, N. J., 2002, 3D geologic modeling and fracture interpretation of the Tensleep Sandstone, Alcova Anticline, Wyoming: M.S. thesis, Colorado School of Mines.

Khaidukov, V., E. Landa, and T. J. Moser, 2004, Diffraction imaging by focusing-defocusing: An outlook on seismic superresolution: Geophysics, **69**, 1478–1490, doi: 10.1190/1.1836821.

Klokov, A., R. Baina, E. Landa, P. Thore, and I. Tarrass, 2010, Diffraction imaging for fracture detection: Synthetic case study: 80th Annual International Meeting, SEG, Expanded Abstracts, 3354–3358.

Klokov, A., and S. Fomel, 2012, Separation and imaging of seismic diffractions using migrated dip-angle gathers: Geophysics, **77**, no. 6, S131–S143, doi: 10.1190/geo2012-0017.1.

Koren, Z., and I. Ravve, 2011, Full-azimuth subsurface angle domain wavefield decomposition and imaging Part I: Directional and reflection image gathers: Geophysics, **76**, no. 1, S1–S13, doi: 10.1190/1.3511352.

Kozlov, E., N. Barasky, E. Korolev, A. Antonenko, and E. Koshchuk, 2004, Imaging scattering objects masked by specular reflections: 74th Annual International Meeting, SEG, Expanded Abstracts, 1131–1134.

Landa, E., S. Fomel, and M. Reshef, 2008, Separation, imaging, and velocity analysis of seismic diffractions using migrated dip-angle gathers: 78th Annual International Meeting, SEG, Expanded Abstracts, 2176–2180.

Milliken, M., and B. Black, 2006, Surface geologic mapping, seismic, and well data resolve complex faulting at Teapot Dome Field, Wyoming: Presented at the Wyoming Geological Association Field Conference.

Moser, T. J., 2009, Diffraction imaging in subsalt geometries and a new look at the scope of reflectivity: Presented at the Subsalt Imaging Workshop: Focus on Azimuth.

Moser, T. J., and C. B. Howard, 2008, Diffraction imaging in depth: Geophysical Prospecting, **56**, 627–641, doi: 10.1111/j.1365-2478.2007.00718.x.

Picard, M. D., 1993, The early Mesozoic history of Wyoming, *in* A. W. Snoke, J. R. Steidmann, and S. M. Roberts, eds., Geology of Wyoming: Wyoming State Geological Survey, Memoir **5**, 210–249.

Popovici, A., T. J. Moser, and I. Sturzu, 2014, Diffraction imaging delineates small-scale natural fractures: American Oil and Gas Reporter, **57**, 89–93.

Raeuchle, S., D. Fernando, E. Duffey, and R. Talbert, 2006, New potential in an existing giant field: Teapot Dome, Wyoming, http://www.searchanddiscovery.com/documents/2006/06027raeuchle/images/raeuchle.pdf, accessed 07 August 2014.

Sturzu, I., A. M. Popovici, and T. J. Moser, 2014, Diffraction imaging using specularity gathers: Journal of Seismic Exploration, **23**, 1–18.

Sturzu, I., A. M. Popovici, N. Tanushev, I. Musat, M. A. Pelissier, and T. J. Moser, 2013, Specularity gathers for diffraction imaging: 75th Annual International Conference and Exhibition, EAGE, Extended Abstracts.

Alexander Mihai Popovici received an equivalent B.S. (1985) in geophysical and geologic engineering from the University of Bucharest, Romania, and an M.Sc. (1991) and a Ph.D. (1995) in geophysics from Stanford University. He escaped from Romania in 1986 and spent a year in a refugee camp in Austria. He is a chief executive officer and chairman at Z-Terra Inc., a provider of state-of-the-art geophysical and geological technology, services, and software for the upstream oil and gas industry. He was a cofounder and CEO of 3DGeo Inc. His industrial experience includes work in the seismic processing research department for Halliburton Geophysical Services in Dallas and Houston, and EM acquisition and processing in Romania. From 1987 to 1983, he was employed at Guzik Technical as a staff engineer for magnetic recording and software development. He has several patents in the field, more than 70 publications in conference proceedings, books, trade journals, and research reports. He has given numerous invited talks at conferences, geophysical associations, and geophysic workshops. He has been a member of the SEG Research Committee, served as an associate editor (Seismic Migration) for Geophysics, and is a past chairman and founding board member of Geoscientists Without Borders, an SEG Foundation program that funds humanitarian applications of geophysics around the world. Currently, he serves on the SEG Foundation Development Board.

Sudha Sudhakar has more than 34 years of experience in the oil and gas industry. He was the founding member of Coherence Technology and has spent eight years working as a geophysicist for oil companies, where he gained interpretation and well planning expertise domestically and internationally. He holds two patents and numerous publications. Currently, he works with Vector Seismic and manages the imaging and reservoir characterization group.

Tijmen Jan Moser received a Ph.D. from Utrecht University and has worked as a geophysical consultant for many companies and institutes (Amoco, Institut Français du Pétrole, Karlsruhe University, Bergen University, Norsk Hydro, Geophysical Institute of Israel, Fugro-Jason, Horizon Energy Partners, Statoil). For several years, he has been working as an independent consultant. His research interests include seismic imaging, asymptotic methods, and diffractions, where he has authored many influential papers. He is the editor-in-chief of *Geophysical Prospecting*, member of SEG and MAA, and honorary member of EAGE.

Ioan Sturzu received a B.S. in engineering physics and an M.S. and a Ph.D. in theoretical physics from the University of Bucharest, Romania. He is a scientific developer at Z-Terra Inc. He is a senior researcher with more than 22 years of experience in academic and industrial environment. His areas of geophysical expertise include diffraction imaging, seismic data processing, seismic data clustering/data segmentation, time/depth migration, multiple attenuation, processing of blended seismic data, wave propagation in heterogeneous media, independent-component analysis, and nonnegative-matrix factorization.